

A NOVEL SHAPE-AWARE TOPOLOGICAL REPRESENTATION FOR GPR DATA WITH DNN INTEGRATION

MEIYAN KANG, SHIZUO KAJI, SANG-YUN LEE, TAEGON KIM,
HEE-HWAN RYU, AND SUYOUNG CHOI

ABSTRACT. Ground Penetrating Radar (GPR) is a widely used non-destructive testing (NDT) technique for subsurface exploration, particularly in infrastructure inspection and maintenance. However, traditional interpretation methods often suffer from noise sensitivity and limited structural awareness.

This study presents a novel framework that integrates shape-aware topological features—derived from B-scan GPR images using Topological Data Analysis (TDA)—with the object detection capabilities of a YOLOv5-based deep neural network (DNN). The proposed topological representation enhances the geometric salience of buried objects, improving the model’s ability to detect and localize underground utilities, especially pipelines.

To mitigate the scarcity of annotated real-world data, a Sim2Real strategy is employed. Synthetic datasets are generated to simulate diverse subsurface conditions, enabling effective knowledge transfer to real-world scenarios.

Experimental results show consistent improvements in mean Average Precision (mAP), highlighting the robustness and effectiveness of the proposed method. This work demonstrates the potential of TDA-enhanced deep learning for reliable subsurface object detection with broad implications in urban planning, safety inspection, and infrastructure management.

1. INTRODUCTION

Inspection of subsurface infrastructure—particularly pipelines—is critical for maintaining urban environments and preventing failures [1]. This task necessitates high-accuracy non-destructive testing (NDT) methods [2]. Among these, *Ground Penetrating Radar (GPR)* has emerged as a widely adopted geophysical technique, facilitating the detection and imaging of subsurface

Date: July 14, 2025.

Key words and phrases. Ground Penetrating Radar (GPR), Topological Data Analysis (TDA), Deep Neural Network (DNN), Object Detection, Sim2Real, Infrastructure Inspection, Pipeline Detection.

This research was supported by Basic Science Research Program through the National Research Foundation of Korea (NRF) (RS-2021-NR060141) and Korea Electric Power Corporation (R21SA02). The second author is partially supported by JST Moonshot R&D Grant Number JPMJMS2021 and the commissioned research (No.22301) by NICT, Japan.

structures across diverse domains such as archaeology, civil engineering, and environmental studies [3, 4]. GPR operates by transmitting electromagnetic waves into the ground and interpreting the resulting reflections to infer subsurface compositions.

Traditionally, the interpretation of GPR signals has relied heavily on manual analysis and physics-based models. These conventional approaches are not only time-consuming and labor-intensive, but also highly susceptible to noise and environmental variability. Such limitations have motivated the exploration of automated solutions. Recent advances in deep learning have driven a paradigm shift in GPR data analysis, enabling significant improvements in automation, detection accuracy, and efficiency. Notably, object detection models—including YOLO (You Only Look Once) [5], Faster R-CNN [6], and U-Net [7]—have demonstrated considerable promise. YOLO excels in rapid classification of subsurface anomalies (e.g., pipelines, voids), requiring minimal post-processing. In contrast, Faster R-CNN often achieves higher accuracy, especially for small or low-contrast objects, but at the cost of increased computational demands, though it typically incurs greater computational cost [8]. U-Net is particularly effective for pixel-level segmentation, aiding in the delineation of complex subsurface structures, though it is prone to overfitting when annotated data is scarce.

Beyond individual model architectures, recent research has explored integrated frameworks for GPR interpretation. For example, Lei et al. [9] combined deep learning with reverse time migration to improve localization accuracy. Similarly, Su et al. [10] introduced an end-to-end deep learning model for underground utility detection, while Xiong et al. [13] proposed GPR-GAN to augment training via synthetic data generation. In addition, Jafuno et al. [11] applied second-order deep learning models to enhance buried object classification, and Tag et al. [12] demonstrated effective groundwater detection using YOLOv8 on GPR datasets.

Despite these advances, a key limitation persists: the performance of deep learning models is heavily reliant on the availability and diversity of high-quality annotated data. Collecting labeled GPR datasets is expensive and logistically challenging, prompting increased interest in simulation-based training approaches.

Sim-to-Real (Sim2Real) transfer has emerged as a viable solution by enabling models trained on simulated GPR data to generalize to real-world environments [14, 15]. Simulated environments allow for the generation of diverse, labeled, and noise-controlled data representing various subsurface conditions. These approaches help bridge the domain gap between synthetic and field data, improving model generalization and robustness.

Another promising direction lies in improving feature representation. *Topological Data Analysis (TDA)* provides a mathematical framework that captures intrinsic structural patterns often overlooked by conventional methods [16, 17]. TDA is particularly appealing in GPR analysis due to its invariance to coordinate transformations and robustness to noise [18, 19]. Its

core technique, persistent homology, encodes the birth and death of topological features across multiple scales, producing a compact yet expressive representation of data geometry [20].

While previous studies have primarily utilized vectorized persistent homology such as barcodes or persistence diagrams as features for machine learning, this work takes a novel approach: we directly integrate topological features derived from persistent homology with raw B-scan GPR data. This fusion enables the model to learn both spatial textures and underlying shape structures, resulting in richer representations and improved detection performance.

In this paper, we present a deep learning framework that incorporates both Sim2Real training and TDA-based feature augmentation within a deep learning YOLOv5 pipeline. Our method demonstrates improved detection performance, as measured by mean Average Precision(mAP), and offers a robust, scalable solution for subsurface object detection.

The remainder of this paper is organized as follows. Section 2 introduces the fundamental concepts of persistent homology that underpin our approach. Section 3 details the proposed framework, including methodology and implementation. Section 4 presents the experimental setup and reports the results on selected datasets.

2. PERSISTENT HOMOLOGY

Persistent homology is a computational technique within TDA that extracts multi-scale structural features from 2D digital images by analyzing how topological properties evolve across different threshold levels [21].

In the context of 2D image analysis, persistent homology operates on *cubical complexes* constructed directly from pixel grids. A cubical complex for a 2D image is built by treating each pixel as a 2-dimensional cube (square), with edges and vertices forming the 1-dimensional and 0-dimensional cubes respectively [22]. This representation is particularly natural for digital images since it preserves the inherent grid structure without requiring triangulation or point cloud conversion.

The persistent homology computation on 2D images typically proceeds through a *filtration* process based on pixel intensity values. Starting from an empty complex, cubes (pixels) are incrementally added in order of increasing (or decreasing) intensity values, creating a nested sequence of cubical complexes. As this filtration progresses, topological features emerge and vanish: connected components appear when pixels are first added (β_0 features), while loops or holes form when pixel arrangements create enclosed regions (β_1 features). See Figure 1 for illustration.

For each topological feature σ detected during this process, persistent homology records its *birth* time (the intensity value when the feature first

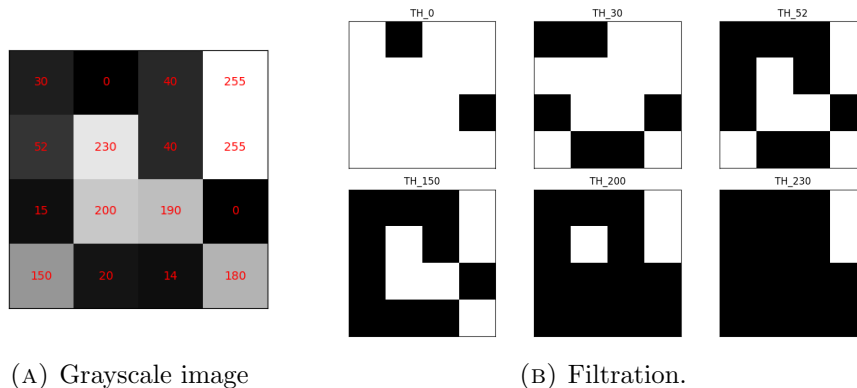


FIGURE 1. Persistent homology applied to grayscale image. (a) A typical grayscale image used for topological analysis. (b) Filtration process for constructing a filtered cubical complex through intensity-based thresholding. As the threshold increases from 0 to 255, pixels are progressively included in the complex.

appears) and *death* time (when it disappears due to subsequent pixel additions). The *lifetime* of the feature is computed as:

$$(1) \quad \text{Lifetime}(\sigma) = \text{Death}(\sigma) - \text{Birth}(\sigma)$$

In 2D image analysis applications, β_0 features (connected components) capture blob-like structures and their hierarchical merging behavior across intensity scales, while β_1 features (loops) identify ring-like or hole structures within the image. Features with long lifetimes typically correspond to significant image structures, whereas short-lived features often represent noise or minor intensity fluctuations. This multi-scale analysis enables robust feature extraction that is less sensitive to noise compared to traditional computer vision approaches, making persistent homology particularly valuable for medical imaging, texture analysis, and shape recognition tasks where topological structure carries important semantic information [23].

3. METHODOLOGY

The aim of this study is to accurately detect underground pipelines using GPR. In particular, we focus on analyzing B-scan images, which are the primary output of GPR measurements. A B-scan represents a two-dimensional cross-sectional image generated by sweeping the radar antenna along a linear path. While B-scan images provide valuable information about subsurface structures, they are often contaminated with noise and clutter, making automated interpretation a challenging task. To address this issue, we propose utilizing TDA to enhance detection performance by extracting robust,

noise-resistant features that capture the inherent shape of the data. Specifically, we capture topological structures embedded in B-scan images, such as loops formed by hyperbolic reflections from buried cylindrical objects. These shape-aware topological features are then fused with the original image data, resulting in enriched structural representations that enhance the model’s sensitivity to object geometry.

3.1. Step 1: Shape-Aware Topological Representation. The core contribution of this study lies in bridging the gap between topological data analysis and convolutional neural networks (CNNs) for enhanced shape-aware object detection. While CNNs excel at capturing local textural patterns, they are inherently biased toward low-level features and struggle to capture global shape information. This limitation is particularly problematic for detecting buried pipelines in GPR imagery, where target objects manifest as distinctive curved, hyperbolic patterns that require global shape understanding rather than local texture analysis.

To address this fundamental limitation, we develop a novel method that enables CNNs to effectively digest topological and global shape information by encoding persistent homology-derived features directly into image representations. Our approach transforms abstract topological annotations into a visual format that CNNs can naturally process, thereby augmenting their shape perception capabilities without requiring architectural modifications.

We treat each B-scan image as a grayscale 2D image and apply the persistent homology framework described in Section 2. We focus exclusively on β_1 topological features (loops), as our primary interest lies in the crescent-shaped closed patterns representing subsurface pipelines.

The key idea of our approach lies in transforming abstract topological information into a format that CNNs can effectively utilize. Rather than relying on conventional persistence diagrams or barcodes, which provide compact summaries but cannot be directly processed by CNNs, we construct a spatial representation that preserves both topological significance and spatial locality. We create a new image with identical dimensions to the original input, visualizing the shapes of degree-one homology generators while modulating their intensity according to their lifetime. Generators with longer lifetimes are rendered with higher intensity, while shorter-lived features appear with lighter shading. This spatial encoding enables CNNs to simultaneously access local pixel information and global topological structure within their standard convolution operations. To construct the final input for the object detection model, we stack the grayscale GPR B-scan image and the lifetime-weighted topological feature map along the channel dimension, forming a multi-channel representation. This approach allows the CNN-based detector (YOLOv5) to learn from both raw spatial information and topological cues, effectively augmenting its shape perception capabilities. The CNN can thus leverage its existing architectural strengths

3.2. Step 2: Sim2Real Training. Collecting and annotating real-world GPR data presents significant challenges, as subsurface environments are inherently complex and buried utilities are difficult to access for accurate ground-truth labeling. This labour-intensive annotation process makes training YOLOv5 directly on large-scale field datasets impractical.

To overcome this data scarcity challenge, we adopt a Sim2Real training philosophy that leverages synthetic data generation followed by real-world fine-tuning. Our approach begins with pre-training the model on a comprehensive dataset of synthetic GPR B-scan images generated using *gprMax*, with the data generation procedure detailed in Section IV. 4.1. These simulated images undergo processing through our TDA pipeline (Section 3.1), where β_1 topological features corresponding to hyperbolic reflections are extracted and encoded into lifetime-weighted shape-aware representations.

This synthetic pre-training phase enables the model to acquire fundamental knowledge of subsurface reflection patterns and their topological signatures without requiring extensive real-world annotations. The enriched synthetic data, augmented with persistent homology features, provides a robust foundation for learning the characteristic shapes and structures associated with buried pipelines.

Following the pre-training phase, the model is fine-tuned using a curated set of real-world GPR scans obtained from a controlled testbed environment. These field data exhibit complex variations due to factors such as soil heterogeneity, depth-dependent signal attenuation, and sensor-induced noise. The field data acquisition and experimental setup are detailed in Section 4.2.

Fine-tuning on field data is essential for bridging the domain gap between the idealized conditions of synthetic simulations and the stochastic, site-specific nature of real-world measurements. While pre-training enables the model to learn generalized geometric and topological priors, fine-tuning refines the learned parameters to adapt to real-world complexity. This process enhances the model’s robustness and adaptability, allowing it to detect nuanced subsurface features more effectively. By incorporating a diverse range of field samples, the fine-tuning phase significantly improves real-world performance, enabling reliable detection of buried utilities under challenging and variable environmental conditions.

This two-stage approach maximizes the utility of limited real-world data while leveraging the scalability of synthetic data generation, ultimately achieving robust performance in practical deployment scenarios. The complete training schema is illustrated in Figure 3.

4. EXPERIMENTS AND RESULTS

4.1. Numerical Data Generation. We employed the Finite-Difference Time-Domain (FDTD) method, which discretizes time and space to numerically solve Maxwell’s equations, enabling accurate simulation of electromagnetic wave propagation. For this purpose, we used the open-source

software gprMax, which allows efficient modeling of complex subsurface environments [24].

The simulation setup included essential components such as pipe placement, soil layering, and grid resolution to reflect realistic underground environments. A Ricker wavelet—a zero-phase wavelet commonly used in GPR applications due to its compact time-domain representation—with a 350MHz center frequency was employed as the excitation signal. The radar system was modelled with a co-located transmitter-receiver pair moved in 0.024m increments along the surface, resulting in a total of 456 A-scans (single-point radar measurements) per simulation to construct each B-scan cross-sectional image.

To specify ground material properties accurately, we adopted the Peplinski model [25], which provides empirical relationships for calculating the complex permittivity of soils based on physical parameters such as soil moisture content, bulk density, and particle composition. For enhanced realism, heterogeneous soil conditions were incorporated using a fractal-based stochastic generation algorithm [26], which spatially distributes material properties in a self-similar pattern that mimics natural soil variability. In contrast, homogeneous scenarios assumed constant permittivity values based on averaged water content across the simulation domain.

Table 1 summarizes the key parameters used in the simulation. Pipe diameters ranged from 0.3m to 1.0m, with horizontal positions between 5.0m and 11.0m, and burial depths ranging between 3.5m and 5.3m. Absorbing boundary conditions were applied on all sides with cell padding of [300, 300, 100, 150], corresponding to 1.8, m (left and right), 0.6, m (top), and 0.9, m (bottom), based on the grid resolution of 6, mm.

B-scan images were generated through 2D electromagnetic simulations under both homogeneous and heterogeneous conditions, with scenarios with single and multiple pipes. As shown in Figure 4, wave reflections vary depending on the complexity of subsurface configuration. To improve visibility of deep-layer structures, additional signal post-processing techniques were applied. To further improve the quality of the simulated GPR signals, we applied several signal processing techniques, including background removal (to eliminate static noise), band-pass filtering (to isolate the relevant frequency range), and Automatic Gain Control (AGC) for contrast normalization. The band-pass filter was applied in the frequency range of 100 MHz to 1900 MHz to retain informative signal components while suppressing irrelevant noise. For each B-scan image, five AGC variants were generated to increase the model’s robustness against intensity variations. In total, 1,200 simulated B-scan images were produced. An example output is shown in Figure 4(a).

4.2. Field Data Collection. To evaluate the proposed method under realistic subsurface conditions, GPR B-scan data were collected from three field sites in South Korea:

TABLE 1. Modeling input properties for gprMax simulations

Category	Parameter	Value
Transmission	Wave type	Ricker
	Center frequency (f)	350 MHz
	A-Scan steps (n_{step})	456
	Step-wise movement (Δl_{step})	0.024 m/step
Model Geometry	Model size ($W \times H$)	16.0m \times 6.0 m
	Pipe diameter (D)	[0.3, 0.5, 1.0] m
	Pipe center (x_c, y_c)	([5.0–11.0] m, [3.5–5.3] m)
Grid	Cell size (Δl)	6mm
Boundary	Absorbing BC (BC)	[1.8, 1.8, 0.6, 0.9] m

- **Site A:** 451 Daragjae-ro , Seorak-myeon, Gapyeong-gun, Gyeonggi-do, Republic of Korea
- **Site B:** 2, Busandaehak-ro 63beon-gil, Geumjeong-gu, Busan, Republic of Korea
- **Site C:** 341, Baekbeom-ro, Yongsan-gu, Seoul, Republic of Korea

Each site contains pipes installed at known depths and orientations under heterogeneous soil conditions. Scans were acquired along predefined linear paths using a commercial GPR system developed by Systems, Inc. (USA). The system comprises a main control unit (*SIR 4000*), a 350 MHz antenna (*Model 350HS*), and a survey cart with an encoder wheel (*Model 653*) for accurate distance tracking. This configuration offers a practical trade-off between resolution and penetration depth, and enables consistent data acquisition across sites.

Post-processing was performed using *Radan 7* software. Standard GPR signal processing steps were applied, including background subtraction, band-pass filtering centered around the antenna frequency, and time-varying gain adjustments. These procedures were consistent with those used for simulated data, ensuring a uniform preprocessing pipeline across domains.

Table 2 summarizes the dataset characteristics per site, including image resolution, number of annotated objects, and average bounding box size. A total of 86 B-scan images were collected from Site A, 70 from Site B, and 11 from Site C.

4.3. Model Configurations. To evaluate the effectiveness of the proposed shape-aware topological representation and the Sim2Real training strategy

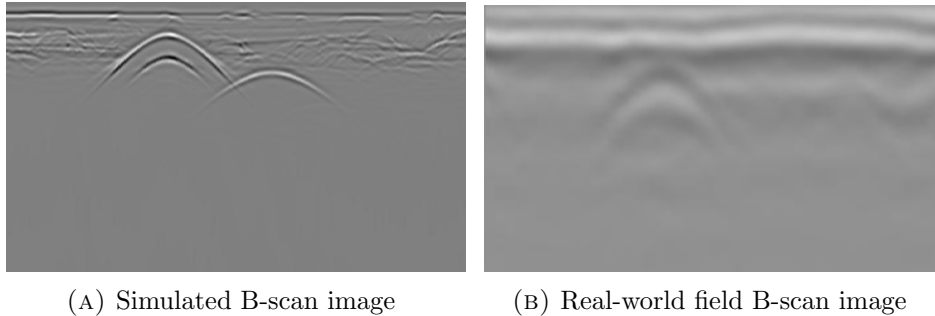


FIGURE 4. Examples of B-scan images used in training. (a) Simulated sample data generated from a synthetic underground model. (b) Field data collected from a controlled testbed environment.

TABLE 2. Descriptive statistics of B-scan datasets

Site	Res. (px)	#Img/Box	Avg. Box (px)
Simulated	1080×1080	300/300	280±33 × 167±43
Site A	680×680	86/94	390±87 × 107±23
Site B	680×680	70/70	234±53 × 79±19
Site C	680×680	11/13	323±134 × 129±38

in object detection, we constructed six distinct model configurations, each designed to isolate the impact of sim2real, topological shape-aware representation, or their combination.

The simulated dataset consists of 300 synthetically generated samples and is used exclusively as a unified training set without partitioning. In contrast, the field dataset comprises 156 real-world samples collected from Site A and Site B, and is employed in a five-fold cross-validation scheme to ensure statistical robustness and consistency. Specifically, the field dataset is divided into five disjoint subsets $\{F^{(i)}\}_{i=1}^5$. For each fold, one subset $F^{(*)}$ is selected as the validation set, and the remaining four subsets are used for training:

$$(2) \quad F_{\text{val}} = F^{(*)}, \quad F_{\text{tr}} = \bigcup_{j \neq *} F^{(j)},$$

where $* \in \{1, 2, 3, 4, 5\}$ denotes the fold index for the current validation set. These notations and data splits are consistently applied across all configurations to ensure fair comparison. In addition, 11 real-world samples from Site C are employed as test dataset.

We define six model configurations: *Base*, *Sim*, *S2R*, *TE-Base*, *TE-Sim*, and *TE-S2R*. Model Base is trained solely on real field data F_{tr} , while

TABLE 3. Model configurations and dataset composition

Model	Training Data	Validation Data	Test Data
Base	F_{tr}	F_{val}	F_{test}
Sim	S_{total}	F_{val}	F_{test}
S2R	Pre-trained: S_{total} Fine-tuned: F_{tr}	F_{val}	F_{test}
TE-Base	\tilde{F}_{tr}	\tilde{F}_{val}	\tilde{F}_{test}
TE-Sim	\tilde{S}_{total}	\tilde{F}_{val}	\tilde{F}_{test}
TE-S2R	Pre-trained: \tilde{S}_{total} (Proposed) Fine-tuned: \tilde{F}_{tr}	\tilde{F}_{val}	\tilde{F}_{test}

Model Sim is trained exclusively on simulated data. Model S2R adopts a domain adaptation approach by pre-training on simulated data and subsequently fine-tuning on field data, aiming to mitigate the domain gap between synthetic and real-world distributions. Model TE-Base, Model TE-Sim, and Model TE-S2R are the shape-aware counterparts of Model Base, Model Sim, and Model S2R, respectively. In the shape-aware configurations, all datasets—including training, validation, and test—are augmented with topological features extracted via persistent homology. These enhanced datasets are denoted with a tilde (e.g., \tilde{F}_{tr} , \tilde{S}_{total}) to indicate the inclusion of shape-aware structural descriptors.

Among all, Model TE-S2R integrates both Sim2Real transfer learning and topological augmentation, and is regarded as the proposed model in this study due to its comprehensive design and superior performance across evaluation metrics.

Table 3 summarizes the training, validation, and test dataset compositions used in each configuration, highlighting the combinations of data sources and the presence or absence of topological augmentation. For clarity, we denote the real-world field dataset by F , with subsets F_{tr} , F_{val} , and F_{test} representing the training, validation, and test splits, respectively. Similarly, S_{total} refers to the full set of simulated samples used for training-only purposes. Tilde symbols (e.g., \tilde{F}_{tr} , \tilde{S}_{total}) indicate that the corresponding data have been augmented with topological features extracted via persistent homology.

4.4. Training Setup. We employed the YOLOv5s architecture, a lightweight and computationally efficient variant of the YOLOv5 family with approximately 7 million parameters. Its fast inference speed and reduced memory footprint make it suitable for GPR-based object detection where real-time performance and hardware efficiency are desired. All models were

trained using consistent hyperparameters based on the YOLOv5s architecture. All input images were resized to 416×416 to comply with the model’s fixed input resolution. The training process differs by configuration:

For training or pre-training, we employed the following hyperparameters:

- **Model config:** yolov5s.yaml
- **Pre-trained weights:** yolo5s.pt
- **Input resolution:** 416×416 pixels
- **Batch size:** 16
- **Training epochs:** 100
- **Optimizer:** SGD with momentum = 0.937, weight decay = 0.0005
- **Learning rate:** Linearly decayed from 0.01 to 0.0001
- **Warmup:** 3-epoch linear warmup increasing learning rate (from 0 to 0.01) and momentum (from 0.8 to 0.937); bias LR starts at 0.1
- **Data augmentation:** Mosaic (probability = 1.0), random horizontal flipping (probability = 0.5), HSV augmentation (hue = 0.015, saturation = 0.7, value = 0.4), translation (0.1), scaling (0.5)
- **Loss function:** Binary cross entropy for classification and objectness, IoU loss for box regression (box = 0.05, cls = 0.5, iou_t = 0.2)
- **Anchor optimization:** Auto-anchor enabled with anchor_t = 4.0 for optimal anchor matching

For fine-tuning, we initialized the model with pre-trained weights and applied the following settings:

- **Model config:** yolov5s.yaml
- **Pre-trained weights:** Pre-trained weights from simulated GPR data (*best.pt*)
- **Optimizer:** SGD with momentum = 0.937, weight decay = 0.0005
- **Learning rate:** Linearly decayed from 0.01 to 0.0001
- **Batch size:** 16
- **Input resolution:** 416×416 pixels
- **Training epochs:** 100
- **Frozen layers:** None (all layers were trainable)
- **Data augmentation:** Mosaic (probability = 1.0), random horizontal flipping (probability = 0.5), HSV augmentation (hue = 0.015, saturation = 0.7, value = 0.4), translation (0.1), scaling (0.5)

Although fine-tuning commonly involves smaller learning rates, shorter training durations and several frozen layers, we observed that retaining the original learning schedule yielded more stable convergence and better generalization in our case, possibly due to the domain gap between simulated and field data, as well as the strong regularization effects from extensive data augmentation. All experiments were conducted using PyTorch 2.7.1 with CUDA 12.7 on a workstation equipped with a single NVIDIA GeForce RTX 4060 GPU (8 GB VRAM).

TABLE 4. Performance comparison across six configurations using 5-fold cross-validation (mean \pm std). Results are reported separately for validation and test sets.

Model	mAP@0.5 (Val)	mAP@0.5 (Test)	mAP@0.5:0.9 (Val)	mAP@0.5:0.9 (Test)	Precision (Val)	Precision (Test)	Recall (Val)	Recall (Test)
Base	0.985 \pm 0.010	0.494 \pm 0.090	0.559 \pm 0.049	0.190 \pm 0.016	0.984 \pm 0.020	0.917 \pm 0.156	0.963 \pm 0.024	0.41 \pm 0.11
Sim	0.276 \pm 0.087	0.031 \pm 0.037	0.138 \pm 0.054	0.013 \pm 0.015	0.311 \pm 0.070	0.024 \pm 0.030	0.204 \pm 0.070	0.062 \pm 0.069
S2R	0.992 \pm 0.003	0.591 \pm 0.097	0.693 \pm 0.007	0.274 \pm 0.025	0.970 \pm 0.016	0.894 \pm 0.080	0.993 \pm 0.014	0.374 \pm 0.126
TE-Base	0.986 \pm 0.009	0.357 \pm 0.089	0.677 \pm 0.031	0.115 \pm 0.028	0.9649 \pm 0.037	0.787 \pm 0.220	0.9774 \pm 0.0201	0.293 \pm 0.035
TE-Sim	0.386 \pm 0.119	0.110 \pm 0.065	0.130 \pm 0.021	0.051 \pm 0.029	0.411 \pm 0.281	0.387 \pm 0.410	0.378 \pm 0.147	0.108 \pm 0.037
TE-S2R	0.990 \pm 0.003	0.643 \pm 0.069	0.704 \pm 0.012	0.306 \pm 0.046	0.967 \pm 0.022	0.918 \pm 0.054	0.988 \pm 0.025	0.456 \pm 0.057

4.5. Results and Comparison. To evaluate detection performance, we compute standard object detection metrics: *Precision*, *Recall*, *mAP@0.5*, and *mAP@0.5:0.95* on validation and test set. *Precision* and *Recall* are used to evaluate the binary detection task of identifying buried pipes. *Precision* represents the proportion of predicted boxes that correctly match actual buried targets, while *Recall* quantifies the proportion of true buried objects that are successfully detected.

Ground truth bounding boxes are generated differently depending on the data source. For simulated data, exact object positions are predefined in the gprMax configuration. For field data, ground truth annotations are based on measured burial depths and object dimensions recorded on the drawing. These annotations serve as ground truth for evaluating detection performance.

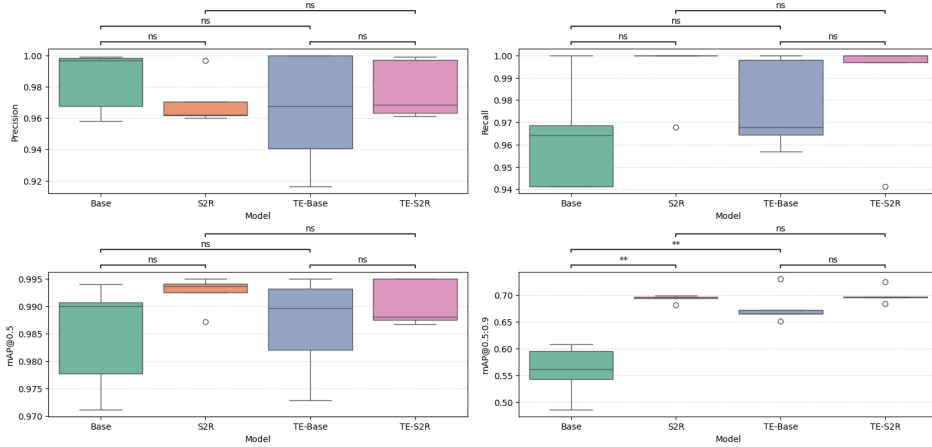
A predicted bounding box is considered correct if its Intersection over Union (IoU) with a ground truth box exceeds a specified threshold 0.6. Matching is based on IoU overlap, and unmatched or duplicate predictions are penalized. This matching protocol is applied consistently across both simulated and real domains.

Tables 4 provides the final 5-fold cross-validation results on the validation and test sets. These results allow for an in-depth evaluation of each configuration’s generalization capability under domain shift conditions.

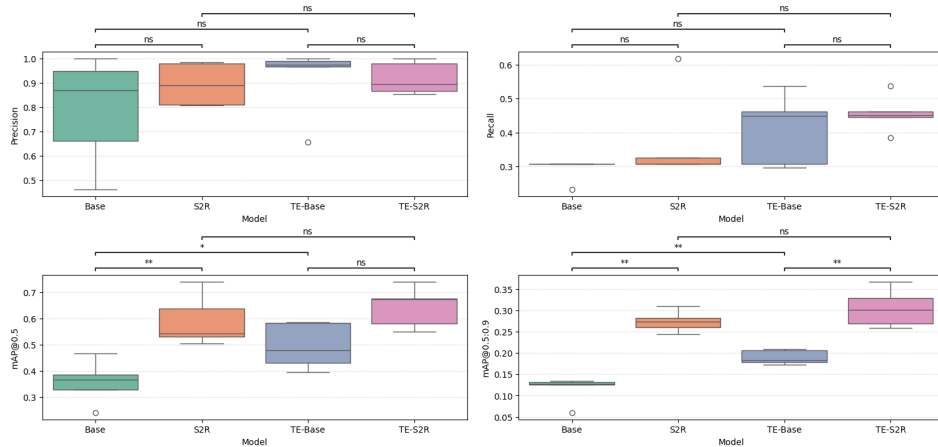
Model Sim and Model TE-Sim, which are trained solely on simulated data, exhibit significantly degraded performance on the test set compared to the validation set. This decline highlights a substantial domain gap between synthetic and real-world data, and underscores the limited generalization ability of models trained exclusively on simulation.

To better understand the individual contributions of the Sim2Real strategy and the proposed shape-aware topological representation, we conducted an ablation study focusing on Model *Base*, Model S2R, Model TE-Base, and Model TE-S2R. The results are illustrated in Fig. 5 (a) and Fig. 5 (b), corresponding to the validation and test sets, respectively.

Across both validation and test results, we observe two consistent trends. First, comparisons between Model *Base* and Model S2R, as well as Model TE-Base and Model TE-S2R, highlight the effectiveness of Sim2Real transfer



(A) Ablation study on validation dataset



(B) Ablation study on test dataset

FIGURE 5. Ablation study evaluating the individual contributions of Sim2Real transfer learning and shape-aware topological augmentation (TDA). Models (a)–(f) correspond to the configurations in Table 3. Mann–Whitney U test was applied to assess statistical significance. Annotations indicate: ‘**’ for $p < 0.01$, ‘*’ for $p < 0.05$, and ‘ns’ for $p \geq 0.05$.

learning. Second, performance improvements from Model Base to Model TE-Base, and from Model S2R to Model TE-S2R, demonstrate the benefit of incorporating shape-aware features via TDA. We observe that TDA-enhanced configurations generally outperform their non-TDA counterparts, particularly under domain shift conditions. This robustness arises because topological features capture global structural patterns that remain stable, even

when local pixel-level intensities vary due to noise, material properties, or sensor inconsistencies.

To assess the statistical significance of these observations, we applied the Mann–Whitney U test to all pairwise comparisons between configurations. The resulting p -values are annotated in the figures using standard notation, where ‘**’ denotes $p < 0.01$ (statistically significant), and ‘ns’ indicates no significant difference ($p \geq 0.05$).

Among all configurations, Model TE-S2R which integrates both Sim2Real and shape-aware topological representation—consistently outperforms the others across all evaluation metrics. This confirms the effectiveness of the proposed approach in improving both accuracy and robustness, particularly under domain shift conditions.

CONCLUSION

This paper presented a novel framework that combines shape-aware topological representations with deep learning-based object detection for GPR data. By incorporating lifetime-weighted persistent homology into the input representation, the proposed method enhances sensitivity to buried object signatures that may be obscured in conventional B-scan images. To the best of our knowledge, this is the first study to incorporate homological information as shape descriptors, marking a significant departure from conventional visual-only representations.

To address domain shift, a Sim2Real strategy was employed—pre-training on simulated data followed by fine-tuning on field data. Experimental results across multiple experiments configurations demonstrated that the TDA-enhanced YOLOv5 model consistently outperformed baseline models in terms of detection accuracy, recall, and precision.

The integration of topological descriptors contributes to both improved generalization and robustness, as these features encode global structural patterns that remain stable across varying environmental factors. This aligns with a well-known strength of topological data analysis (TDA), its ability to capture intrinsic shape information that remains invariant under noise, deformation, and other local perturbations. By relying on the topology of feature space rather than raw pixel intensities, the proposed method maintains stable performance even under challenging real-world GPR conditions.

These results suggest that topological priors can serve as a powerful complement to conventional visual features in GPR-based sensing. Furthermore, the framework may have broader implications beyond geophysical applications—such as biomedical imaging, where structural information is critical but often obscured by noise or intensity variations.

Future work will focus on extending the framework to multi-class scenarios, exploring self-supervised topological learning, and validating performance in broader geophysical environments.

ACKNOWLEDGMENTS

This research was supported by Basic Science Research Program through the National Research Foundation of Korea(NRF) (RS-2021-NR060141) and Korea Electric Power Corporation (R21SA02). The second author is partially supported by JST Moonshot R&D Grant Number JPMJMS2021 and the commissioned research (No.22301) by NICT, Japan.

REFERENCES

- [1] G. Yang, D. Yuan, T. Xu, and B. Li, “An adaptive clutter-immune method for pipeline detection with gpr,” *IEEE Sensors Journal*, vol. 23, no. 19, pp. 22984–22997, 2023.
- [2] A. Neal, “Ground-penetrating radar and its use in sedimentology: principles, problems and progress,” *Earth-Sci. Rev.*, vol. 66, no. 3-4, pp. 261–330, 2004.
- [3] D. J. Daniels, *Ground penetrating radar*. Iet, 2004, vol. 1.
- [4] H. M. Jol, *Ground penetrating radar theory and applications*. Elsevier, 2008.
- [5] J. Redmon, S. Divvala, R. Girshick, and A. Farhadi, “You only look once: Unified, real-time object detection,” in *Proc. IEEE Conf. Comput. Vis. Pattern Recognit. (CVPR)*, 2016, pp. 779–788.
- [6] S. Ren, K. He, R. Girshick, and J. Sun, “Faster r-cnn: Towards real-time object detection with region proposal networks,” *IEEE Trans. Geosci. Remote Sens.*, vol. 39, no. 6, pp. 1137–1149, 2016.
- [7] O. Ronneberger, P. Fischer, and T. Brox, “U-net: Convolutional networks for biomedical image segmentation,” in *Proc. Med. Image Comput. Comput.-Assisted Intervent. (MICCAI)*, 2015, pp. 234–241.
- [8] Z. Fang, Z. Shi, X. Wang, and W. Chen, “Roadbed defect detection from ground penetrating radar b-scan data using faster rcnn,” *IOP Conf. Ser.: Earth Environ. Sci.*, vol. 660, no. 1, p. 012020, Feb. 2021.
- [9] J. Lei, H. Fang, Y. Zhu, Z. Chen, X. Wang, B. Xue, M. Yang, and N. Wang, “Gpr detection localization of underground structures based on deep learning and reverse time migration,” *NDT & E Int.*, vol. 143, p. 103043, 2024.
- [10] Y. Su, J. Wang, D. Li, X. Wang, L. Hu, and Y. Kang, “End-to-end deep learning model for underground utilities localization using gpr,” *Autom. Constr.*, vol. 149, p. 104776, 2023.
- [11] D. Jafuno, A. Mian, G. Ginolhac, and N. Stelzenmuller, “Buried Object Classification from GPR Data by using Second Order Deep Learning Models,” in *Proc. IEEE Int. Geosci. Remote Sens. Symp. (IGARSS)*, p. 6513-6516, 2024.
- [12] A. Tag, O. Shouman, E. Heggy, and T. Khattab, “Automatic Groundwater Detection from GPR Data using YOLOv8,” in *Proc. IEEE Int. Geosci. Remote Sens. Symp. (IGARSS)*, p. 8326-8329, 2024.
- [13] H. Xiong, J. Li, Z. Li, and Z. Zhang, “GPR-GAN: A ground-penetrating radar data generative adversarial network,” *IEEE Trans. Geosci. Remote Sens.*, vol. 62, pp. 1–14, 2023.
- [14] K. Raha and K. P. Ray, “Ground Penetrating Radar Model and its Validation using Developed Prototype,” *Wirel. Pers. Commun.*, vol. 135, no. 2, pp. 1233–1244, 2024.
- [15] J. Ge, H. Sun, S. Wei, D. Liu, Y. Yao, Y. Zhang, R. Liu, and S. Liu, “GPR-TransUNet: An improved TransUNet based on self-attention mechanism for ground penetrating radar inversion,” *J. Appl. Geophys.*, vol. 222, p. 105333, 2024.
- [16] H. Edelsbrunner and J. Harer, *Computational Topology: An Introduction*. American Mathematical Society, 2010.
- [17] R. Ghrist, “Barcodes: the persistent topology of data,” *Bull. Amer. Math. Soc.*, vol. 45, no. 1, pp. 61–75, 2008.

- [18] P. Bubenik, “Statistical topological data analysis using persistence landscapes,” *J. Mach. Learn. Res.*, vol. 16, pp. 77–102, 2015.
- [19] L. Wasserman, “Topological data analysis,” *Annu. Rev. Stat. Appl.*, vol. 5, pp. 501–532, 2018.
- [20] F. Chazal and B. Michel, “An introduction to topological data analysis: Fundamental and practical aspects for data scientists,” *Front. Artif. Intell.*, vol. 4, p. 667963, 2021.
- [21] G. Carlsson, “Topology and data,” *Bull. Amer. Math. Soc.*, vol. 46, no. 2, pp. 255–308, 2009.
- [22] T. Kaczynski, K. Mischaikow, and M. Mrozek, *Computational homology*, vol. 157, Applied Mathematical Sciences. New York, NY, USA: Springer, 2004.
- [23] D. A. Brito-Pacheco, C. C. Reyes-Aldasoro, and P. Giannopoulos, “Persistent homology in medical image processing: A literature review,” *medRxiv*, preprint. 2025–02, 2025.
- [24] C. Warren, A. Giannopoulos, and I. Giannakis, “gprmax: Open source software to simulate electromagnetic wave propagation for ground penetrating radar,” *Comput. Phys. Commun.*, vol. 209, pp. 163–170, 2016.
- [25] N. R. Peplinski, F. T. Ulaby, and M. C. Dobson, “Dielectric properties of soils in the 0.3-1.3-ghz range,” *IEEE Trans. Geosci. Remote Sens.*, vol. 33, no. 3, pp. 803–807, 1995.
- [26] F. J. Molz, H. Rajaram, and S. Lu, “Stochastic fractal-based models of heterogeneity in subsurface hydrology: Origins, applications, limitations, and future research questions,” *Reviews of Geophysics*, vol. 42, no. 1, 2004.

DEPARTMENT OF MATHEMATICS, AJOU UNIVERSITY, 206, WORLD CUP-RO, YEONGTONG-GU, SUWON 16499, REPUBLIC OF KOREA

Email address: miyeon@ajou.ac.kr

INSTITUTE OF MATHEMATICS FOR INDUSTRY, KYUSHU UNIVERSITY, FUKUOKA, 819-0395, JAPAN; GRADUATE SCHOOL OF SCIENCE, KYOTO UNIVERSITY, KYOTO, 606-8502, JAPAN

Email address: skaji@imi.kyushu-u.ac.jp

CONSTRUCTION ENVIRONMENT SYSTEM RESEARCH INSTITUTE, INHA UNIVERSITY, INCHEON, 22212, REPUBLIC OF KOREA

Email address: sangyunlee@kict.re.kr

DEPARTMENT OF MATHEMATICS, AJOU UNIVERSITY, 206, WORLD CUP-RO, YEONGTONG-GU, SUWON 16499, REPUBLIC OF KOREA

Email address: nayo6180@gmail.com

TRANSMISSION & SUBSTATION LABORATORY, KOREA ELECTRIC POWER CORPORATION (KEPCO) RESEARCH INSTITUTE, DAEJEON, 34056, REPUBLIC OF KOREA

Email address: hhryu82@kepc.co.kr

DEPARTMENT OF MATHEMATICS, AJOU UNIVERSITY, 206, WORLD CUP-RO, YEONGTONG-GU, SUWON 16499, REPUBLIC OF KOREA

Email address: schoi@ajou.ac.kr